Supplementary Information

How does the metal-promoted In_2O_3 catalyst choose the pathway for CO_2 hydrogenation to methanol?

Linlin Wu, [ab] Rui Zou, [ab] Shilong Xiong,[ab] Menghui Liu, [ab] Yuxiang Yang, [ab],

Donghai Mei,*[c] and Chang-jun Liu*[ab]

[a] *Collaborative Innovation Center of Chemical Science & Engineering, School of Chemical Engineering and Technology, Tianjin University, Tianjin 300350, China*

[b] *State Key Laboratory of Synthetic Biology, Tianjin University, Tianjin 30072, China*

[c] *School of Environmental Science and Engineering, Tiangong University, Tianjin 300387, China*

Corresponding authors.

E-mail addresses: dhmei@tiangong.edu.cn; cjL@tju.edu.cn.

DFT calculations

Periodic DFT calculations in this work were performed using the Vienna *Ab initio* simulation package (VASP 5.4.4), employing the generalized gradient approximation (GGA) with the Perdew-Burke-Ernzerhof (PBE) exchange-correlation functional for the exchange-correlation energy.[S1] The electronic-core interactions were described by the projector augmented wave (PAW) method.[S2] The dispersive interaction correction was carried out by the DFT-D3 method.[S3] Valence states included the 4d, 5s, and 5p orbitals of In and 5d and 6s orbitals of Au. A plane-wave basis set with a kinetic cutoff energy of 400 eV and 3×3×1 Monkhorst-Pack k-points grid was employed. The convergence criteria for the relaxation of atomic structures and the electronically self-consistent iteration were set at 0.03 eV $Å^{-1}$ and 10^{-5} eV, respectively. The spin-polarized GGA was employed to describe the magnetic properties of the Ni clusters.

The climbing image nudged elastic band (CI-NEB) method was used to obtain the initial guess transition state structures[S4] and the structure was further refined by the Dimer method[S5]. The convergence criteria of the forces and the energies on all unconstrained atoms were less than 0.03 eV $Å^{-1}$ and 10^{-7} eV, respectively. The obtained structure was confirmed by frequency analysis.

The (111) facet of c-In_2O_3 was chosen for calculation because it had the highest thermodynamic stability.[S6] The In_2O_3(111) model with three atomic layers contained 72 O and 48 In atoms. A vacuum layer with a thickness of 15 Å was set to eliminate the interaction between the periodically repeated slabs. In this study, we chose the most stable surface oxygen vacancy,[S7] which is generated by removing an O atom from the surface, as shown in Fig. S4a.

The Au_8 isomer was placed in a 15 × 15 × 15 $Å^3$ cubic cell and subjected to geometric optimization.

Au(100) surface was modeled with a five-layer slab with a vacuum thickness of 15 Å, where the top three layers were relaxed while the bottom two layers were fixed.[S8] A 3×3 supercell and a Monkhorst-Pack (3×3×1) k-point mesh were employed for this structure.

All calculated energy values were thermodynamically corrected to the Gibbs free energy using the VASPKIT code.[S9]

The binding energy of the Au_n on the support was defined as

$$G_{bind} = G(Au_n/In_2O_3) - G(Au_n) - G(In_2O_3)$$

where $G(Au_n/In_2O_3)$, $G(Au_n)$ and $G(In_2O_3)$ denote the Gibbs free energy of the Au_n/In_2O_3 model, Au_n and defective $In_2O_3(111)$ surface, respectively.

The adsorption energy was defined as

$$G_{ads} = G_{a/s} - G_s - G_a$$

where $G_{a/s}$, G_s, and G_a represent the Gibbs free energy of the surface slab with the adsorbate, the clean slab, and the free adsorbate, respectively.

Chemical bond strengths were quantified via crystal orbital Hamilton population (COHP) analysis implemented in the LOBSTER package.[S10]

Catalyst preparation

In_2O_3 was synthesized via the precipitation method as described in previous studies.[S11] Au/In_2O_3 catalyst was prepared by the deposition-precipitation method. Initially, 255 μL of chloroauric acid solution ($HAuCl_4$, Jinbolan Fine Chemical Corporation, Tianjin, 0.1 M) was dissolved in 50 mL of deionized water under continuous stirring. Subsequently, 0.495 g of as-prepared In_2O_3 powder was introduced into the above solution under intense stirring for 1 h at room temperature. Next, 0.4 g of urea (Kermel, Tianjin, GR) was added to the slurry following a vigorous stir at 80 °C for 3 h. The resulting mixture was filtered, washed with 1 L of deionized water, and freeze-dried overnight. Au nanoparticle size was controlled by the method described in the literature.[S12] In_2O_3-supported Au nanoclusters ($Au(NC)/In_2O_3$) were obtained after hydrogen reduction in a 10% H_2/Ar stream at 60 °C for 1 h. In_2O_3-supported Au nanoparticles ($Au(NP)/In_2O_3$) were prepared by calcination in static air at 500 °C for 3 h.

Catalyst characterization

An inductively coupled plasma optical emission spectrometer (ICP-OES) was used on an Agilent 5110 to determine the practical loading of Au species.

Powder X-ray diffraction (XRD) patterns were recorded using a Smartlab diffractometer with Cu Kα radiation, scanning at a rate of 4° min^{-1} over the 2θ range from 20° to 80°.

The specific surface area, calculated by the Brunauer-Emmett-Teller (BET) method, was determined from nitrogen sorption isotherms measured on a Micromeritics ASAP 2460 instrument at -196 °C. Before the test, the catalyst was outgassed in a vacuum at 150 °C for 8 h.

CO_2 temperature-programmed desorption (CO_2-TPD) was performed to investigate the adsorption and activation of CO_2 and H_2, respectively. The experiment was carried out by a Micromeritics Autochem II 2920 chemisorption analyzer equipped with an online HPR-20 EGA mass spectrometer. Typically, 100 mg of sample fixed in a U-shaped quartz tube was pretreated in a He flow at 200 °C for 1 h. After being cooled down to 50 °C and saturated with a CO_2 flow for 1 h, the catalyst was purged with He at the same temperature for 60 min to remove physically adsorbed CO_2. TPD was ramped up to 700 °C at a rate of 10 °C min^{-1} under the same gas flow. The signals of CO_2 (m/z = 44) were collected by the mass spectrometer.

In situ diffuse reflectance infrared Fourier transform spectroscopy (DRIFTS) was performed on a Thermos Scientific Nicolet iS50 FT-IR spectrometer equipped with an MCT detector, recorded with a resolution of 4 cm^{-1}. The sample was loaded into a high-temperature reaction cell with a ZnSe window and purged with flowing Ar at 200 °C for 1 h. Then the background spectra were collected, and CO_2 flow (30 mL min^{-1}) was introduced into the reaction cell at the same temperature. Finally, the system pressure was gradually increased from 0.1 MPa to 1.0 MPa, with spectra continuously recorded during this process. All spectra were collected until adsorption saturation was achieved.

X-ray absorption fine structure (XAFS) analysis was performed at the BL11B beamline of the Shanghai Synchrotron Radiation Facility (SSRF). Both X-ray absorption near-edge structure (XANES) and the extended X-ray absorption fine structure (EXAFS) spectra were obtained in fluorescence mode under room temperature and ambient atmosphere conditions. The spectra were analyzed by the Demeter software package (Version 0.9.26).[S13]

High-angle annular dark-field scanning transmission electron microscopy (HAADF-STEM) was performed using an aberration-corrected JEOL ARM 200F operated at an accelerating voltage of 200 kV.

Catalytic activity

The evaluation of CO_2 hydrogenation to methanol was conducted by a vertically oriented fixed-bed tubular microreactor. Normally, a mixture of 0.2 g catalyst and 1 g of carborundum was fixed in the reactor and pretreated in N_2 flow (50 mL min^{-1}) at 200 °C for 30 min before the reaction. Subsequently, a mixed gas containing H_2, CO_2, and N_2 in a volume ratio of 76:19:5 was input into the reactor under a pressure of 5 MPa. The catalytic activity was tested from 200 to 300 °C with a flow rate of 70 mL min^{-1} and a gaseous hourly space velocity (GHSV) of 21,000 mL h^{-1} g_{cat}^{-1}. The online gas chromatograph (Agilent 7890A) equipped with a flame-ionized detector (FID) and a thermal conductivity detector (TCD) was utilized to analyze all the products.

The following equations were employed in CO_2 conversion (X_{CO_2}), selectivity (S_i), and methanol space-time yield (STY) calculations.

$$X_{CO_2} = \frac{F_{CO_2,\,in} - F_{CO_2,\,out}}{F_{CO_2,\,in}} \times 100\%$$

$$S_i = \frac{F_{i,in} - F_{i,out}}{F_{CO_2,in} - F_{CO_2,out}} \times 100\%$$

$$STY = \frac{F_{CO_2,in} \times X_{CO_2} \times S_{CH_3OH}}{m} \times M$$

$$TOF = \frac{F_{CO_2,in} \times X_{CO_2} \times S_{CH_3OH}}{m \times 3600} \times \frac{M_{metal}}{w_{metal}}$$

In the given equations, F_i denotes the molar flow rate of species i, M represents the molar mass of methanol, m signifies the weight of the catalyst, M_{metal} represents the molar mass of metal, and w_{metal} represents the metal loading. During all experiments conducted, data were considered valid only if they adhered to a carbon balance within the range of 100±1%.

Details of reaction pathway for Rh/In_2O_3

The reaction pathway of CO_2 hydrogenation to methanol on the Rh_8/In_2O_3_d model was studied, as shown in Figs. S17 and S18. Firstly, the adsorbed CO_2 can be directly dissociated (CO hydrogenation pathway), hydrogenated to HCOO* (formate pathway), or protonated to COOH* (RWGS pathway). The formation of HCOO* and COOH* needs to overcome activation barriers of 1.16 eV and 0.60 eV, respectively, both of which are higher than the activation barrier of CO_2 direct dissociation (0.20 eV). This suggests that the adsorbed CO_2 on the interfacial site of Rh_8/In_2O_3_d tends to be dissociated directly. The O* fills the Ov while CO* adsorbs on the Rh cluster. This C-O bond cleavage is exothermic (-0.55 eV) with an activation barrier of 0.20 eV, and CO* desorption requires 1.39 eV. Then O* reacts with H* to form OH* with an activation barrier of 1.00 eV. CO* is hydrogenated to HCO* with an activation barrier of 0.70 eV. OH* further reacts with H* to generate H_2O, which desorbs and regenerates the Ov with an activation barrier of 0.97 eV. Then HCO* undergoes sequential hydrogenation to H_2CO* and H_3CO* with activation barriers of 0.64 eV and 0.78 eV, respectively. Finally, H_3CO* is protonated to H_3COH* with an activation barrier of 0.81 eV. This shows that Rh/In_2O_3 takes CO hydrogenation pathway for CO_2 hydrogenation to methanol.

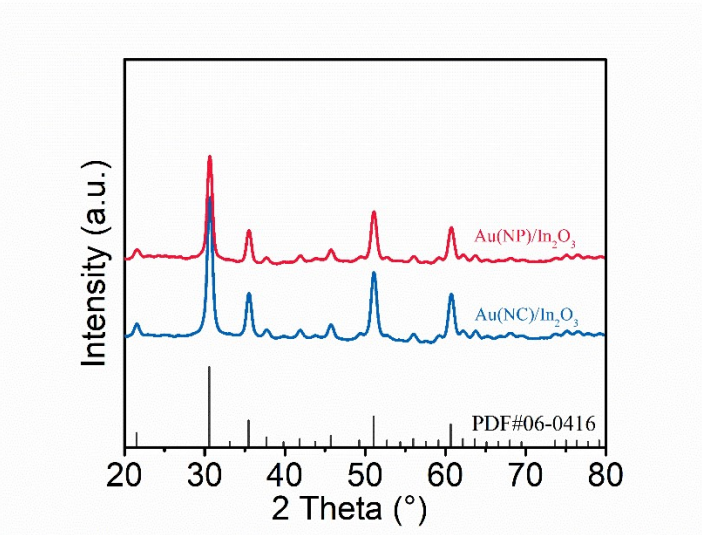

Fig. S1. XRD patterns of Au-promoted In_2O_3 catalysts. The XRD patterns show that except for signals belonging to cubic In_2O_3 (JCPDS No.06-0416), there is no Au diffraction peak observed for Au(NC)/In_2O_3 and Au(NP)/In_2O_3.

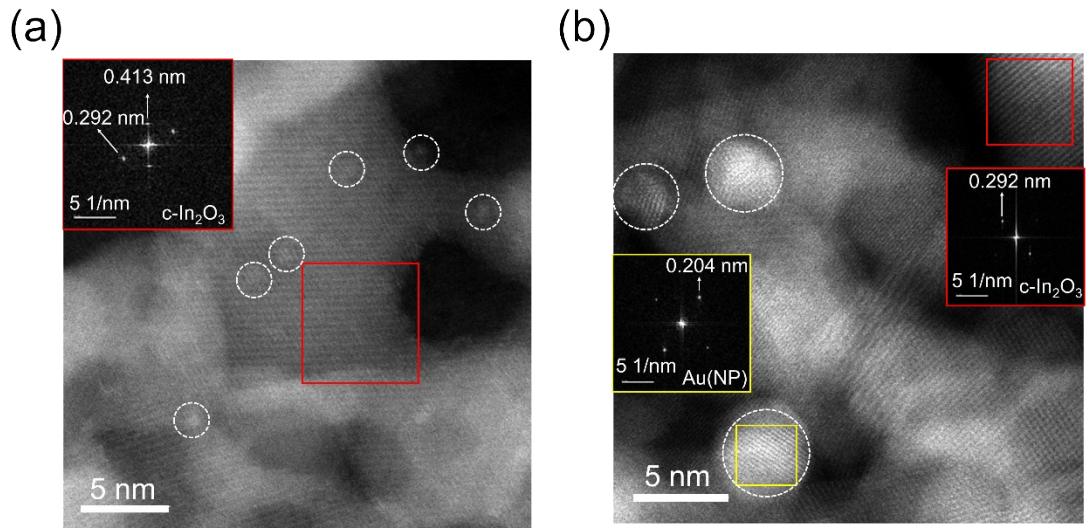

Fig. S2. AC-HAADF-STEM images of (a) Au(NC)/In_2O_3 and (b) Au(NP)/In_2O_3. White circles highlight Au nanoclusters (1.0±0.2 nm) and Au nanoparticles (4.5±0.2 nm), respectively. Fast Fourier Transformation (FFT) pattern of the red-framed region in Fig S6 (a) reveals the (222) and (211) facets of c-In_2O_3 with interplanar spacings of 0.292 nm and 0.413 nm, respectively. In Fig. S6 (b), FFT pattern from the red-framed region shows the (222) facet of c-In_2O_3 (0.292 nm), and FFT pattern of the yellow-framed region corresponds to the (200) facet of Au nanoparticle (0.204 nm).

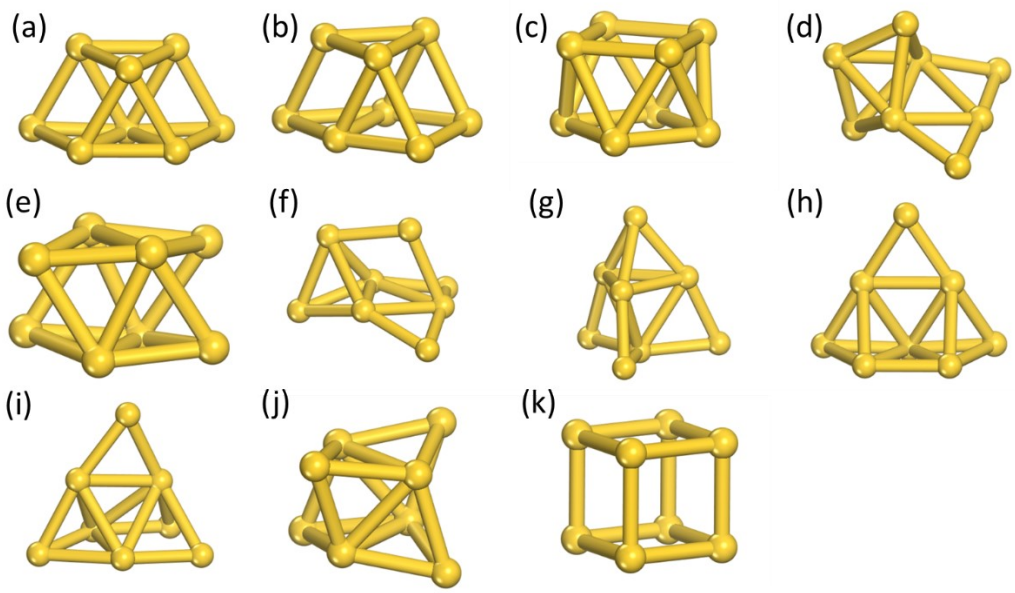

Fig. S3. (a-k) Energetically stable configurations of isolated Au_8 isomers in the gas phase.

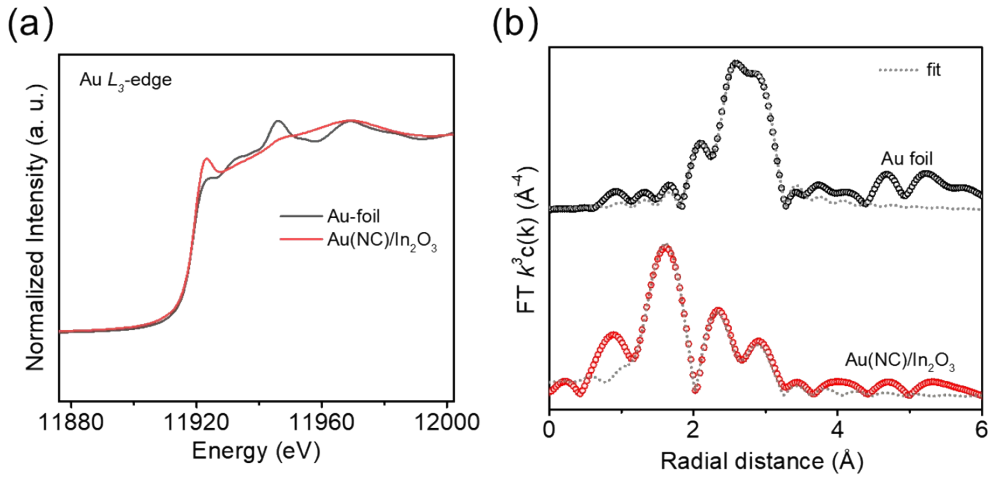

Fig. S4. (a) Normalized Au L_3-edge XANES spectra and (b) k^3-weighted Fourier-transformed EXAFS spectra (without phase-shift correction) of Au foil and Au(NC)/In_2O_3.

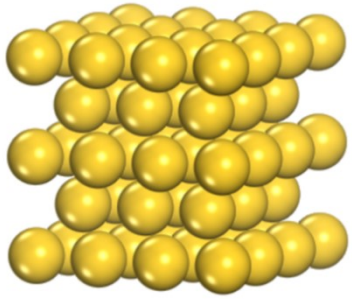

Fig. S5. Energetically stable configurations of clean Au(100) model modeled as p(3×3) slab with five layers in the gas phase.

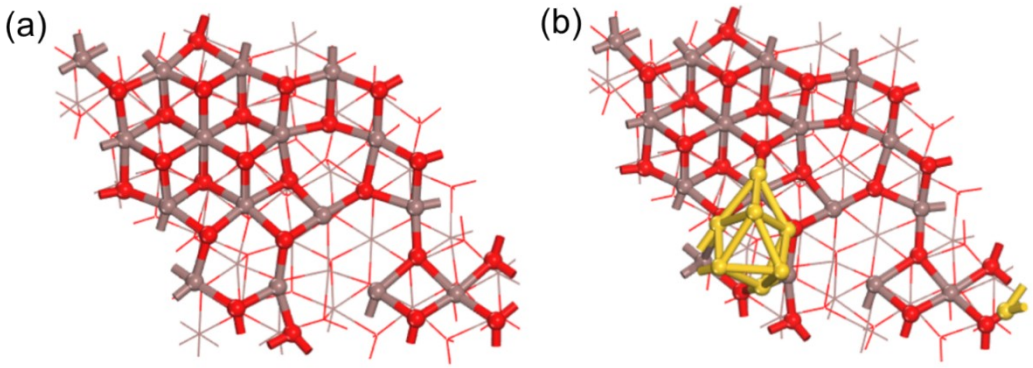

Fig. S6. Optimized configurations of (a) In_2O_3_d, (b) Au_8/In_2O_3_d.

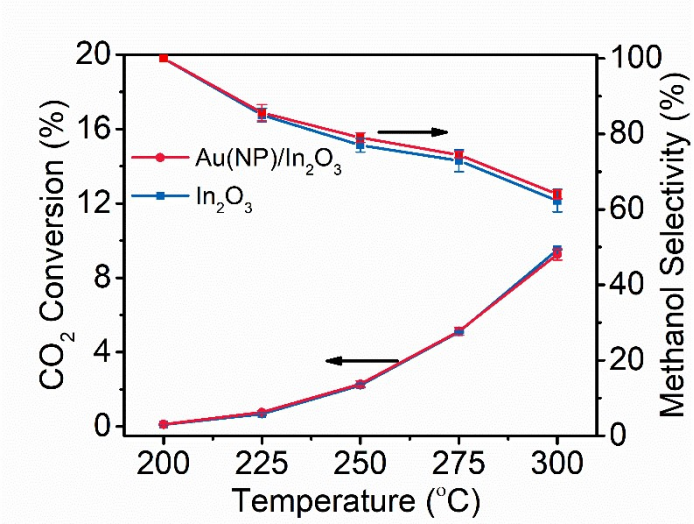

Fig. S7. CO_2 conversion and methanol selectivity of Au(NP)/In_2O_3 and In_2O_3 catalysts in CO_2 hydrogenation to methanol.

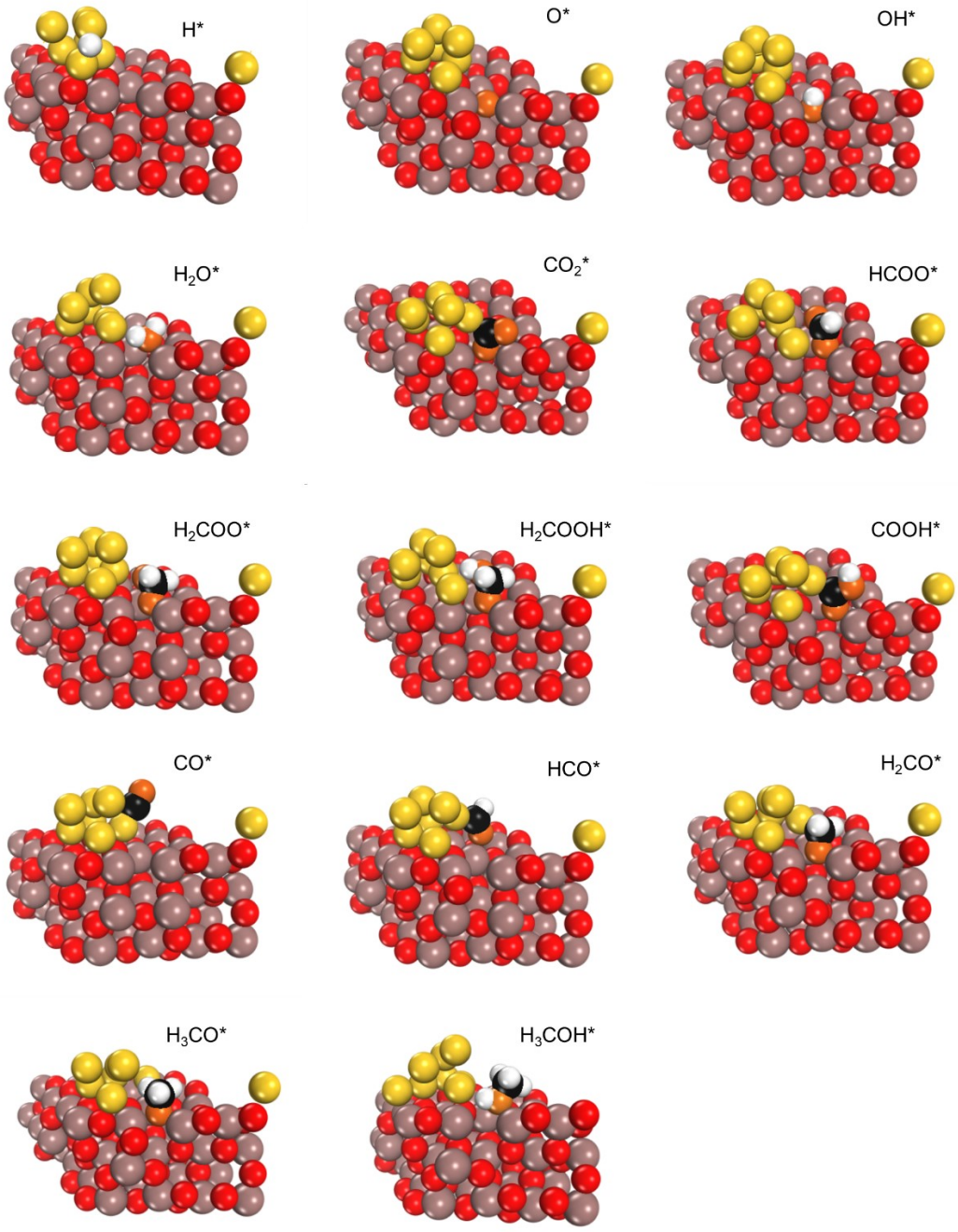

Fig. S8. Optimized configurations of all reaction intermediates absorbed on the surface of Au_8/In_2O_3_d during CO_2 hydrogenation to methanol. Color code: gold (yellow), indium (brown), oxygen in In_2O_3 (red), oxygen in the intermediates (orange), carbon (black), and hydrogen (white).

RWGS:

R1: CO_2*+2H*→COOH*+H*

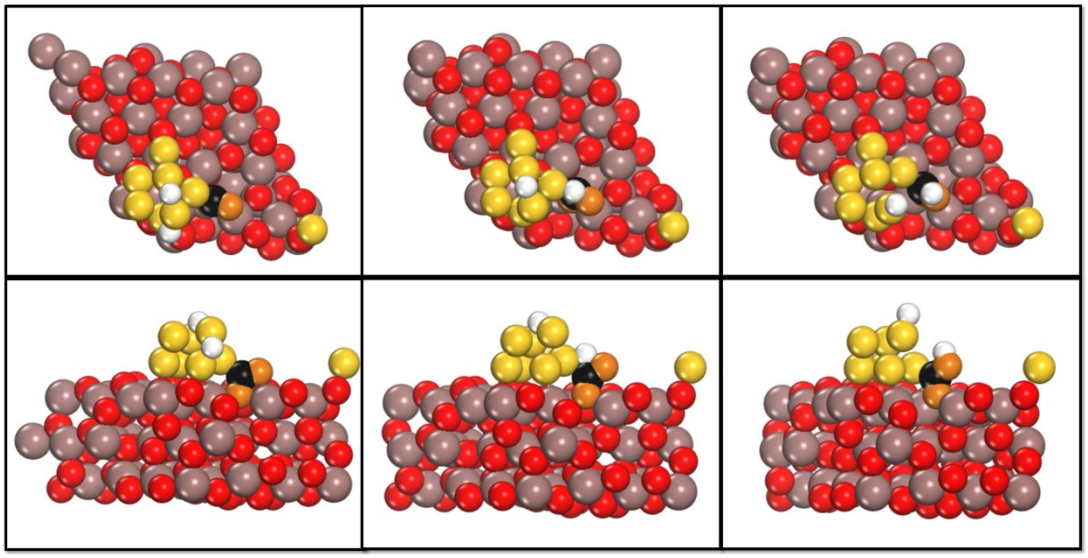

R2: COOH*+H*→CO*+H_2O(g)

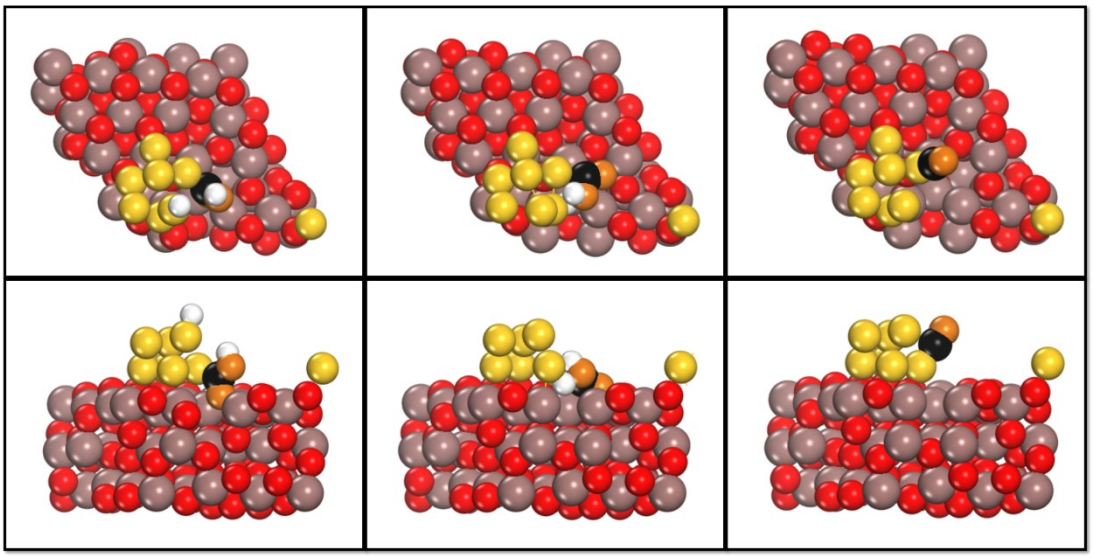

Fig. S9. Optimized configuration for each elementary step along the RWGS pathway over the Au_8/In_2O_3_d model.

Formate:

R3: CO_2*+2H*→HCOO*+H*

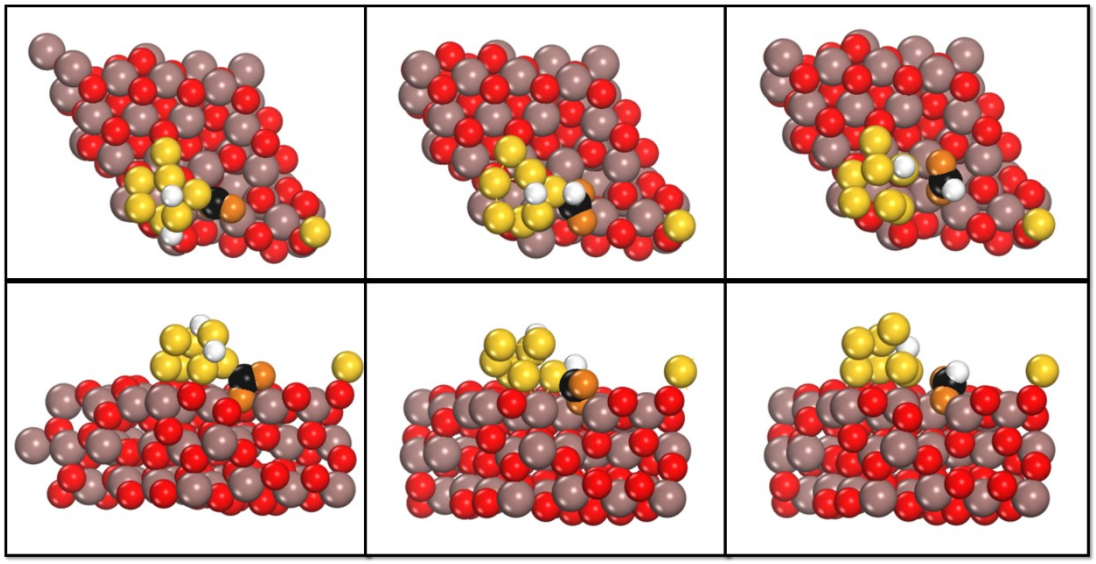

R4: HCOO*+H*→H_2COO*

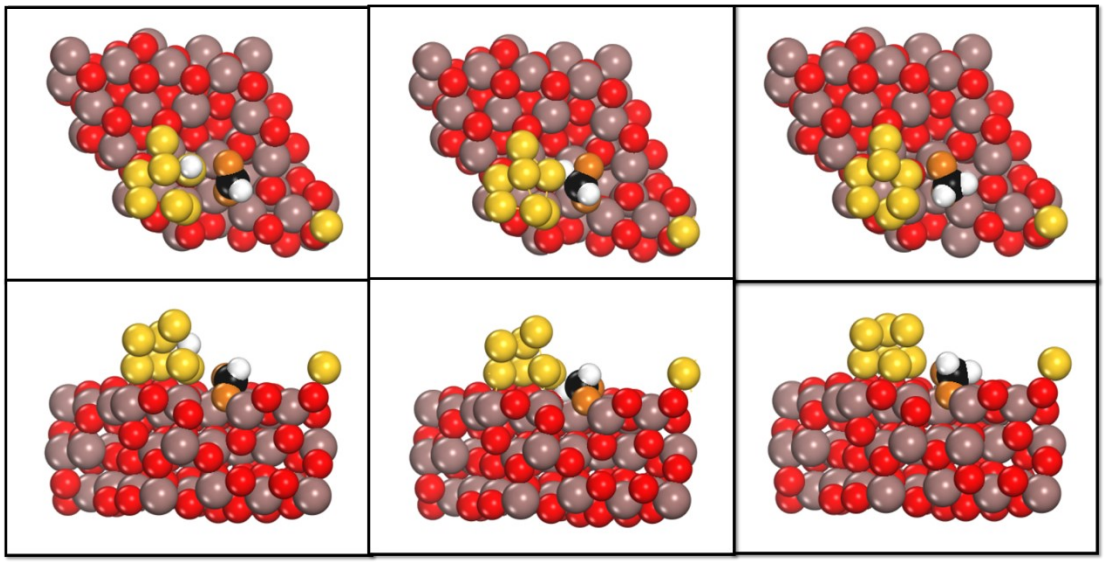

R5: $H_2COO^*+2H^*\rightarrow H_2COOH^*+H^*$

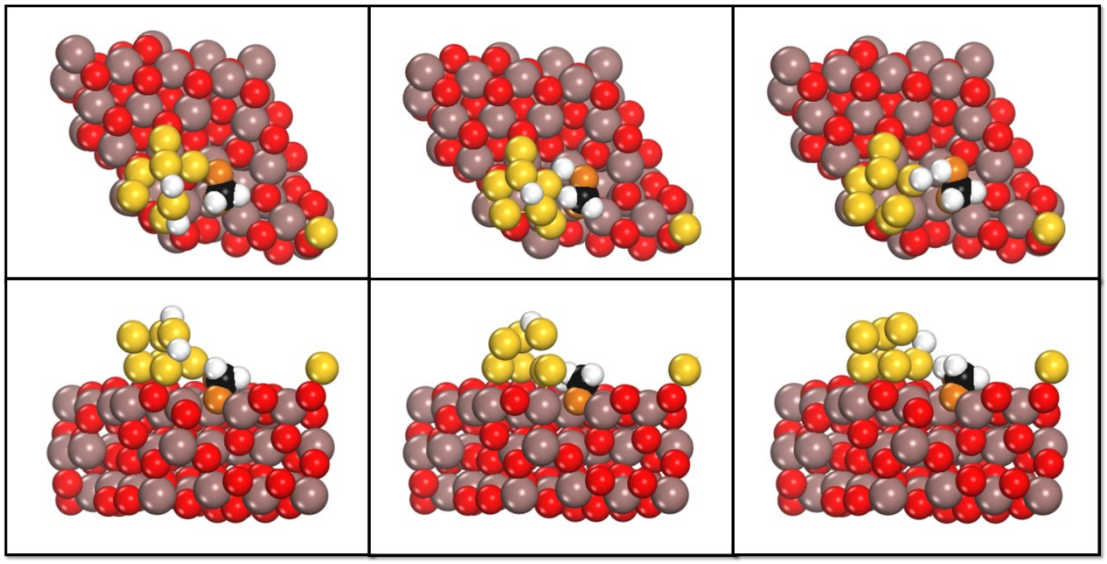

R6: $H_2COOH^*+H^*\rightarrow H_2CO^*+H_2O(g)$

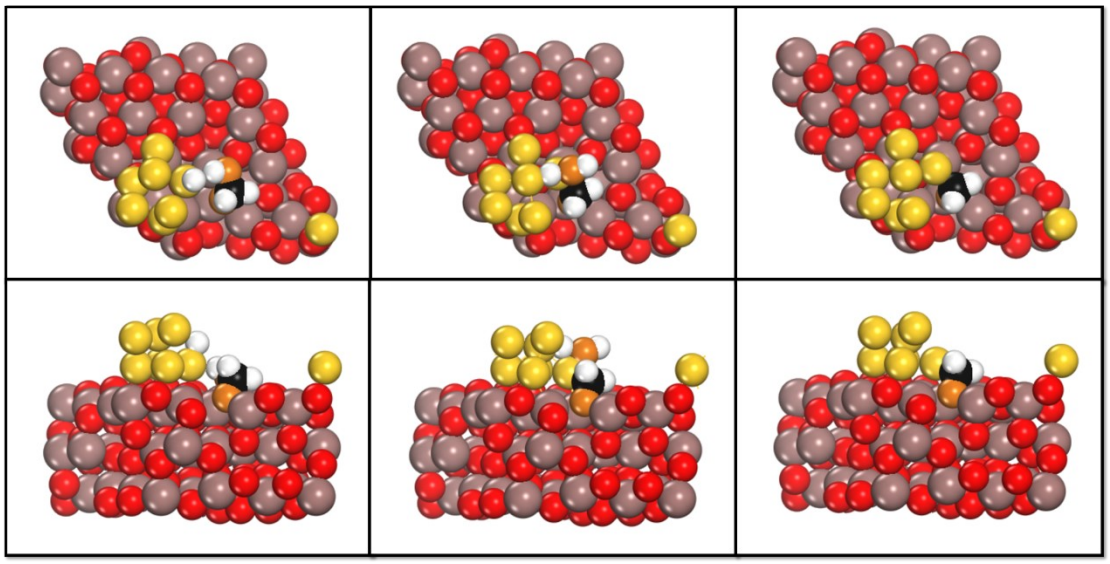

R7: $H_2CO^* + 2H^* \rightarrow H_3CO^* + H^*$

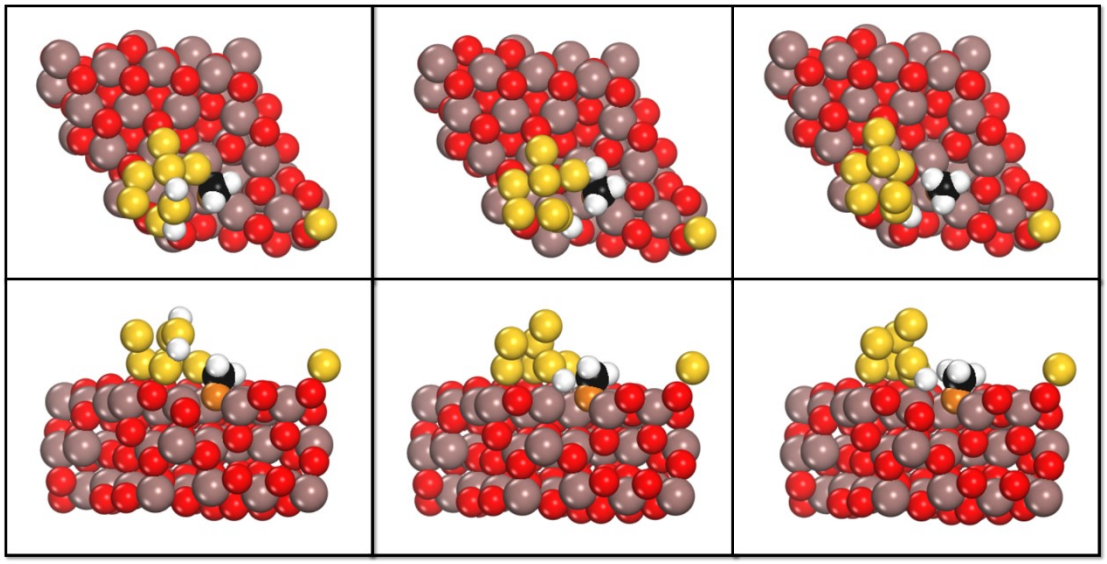

R8: $H_3CO^* + H^* \rightarrow H_3COH^*$

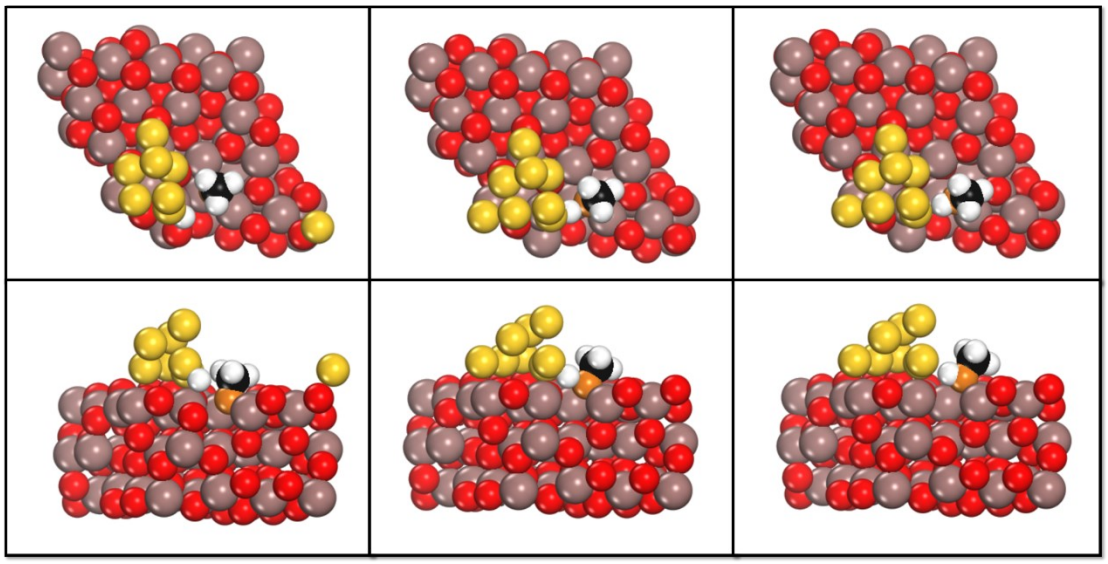

Fig. S10. Optimized configuration for each elementary step along the formate pathway over the Au_8/In_2O_3_d model.

CO-hydrogenation:

R9: CO_2*→CO*+O*

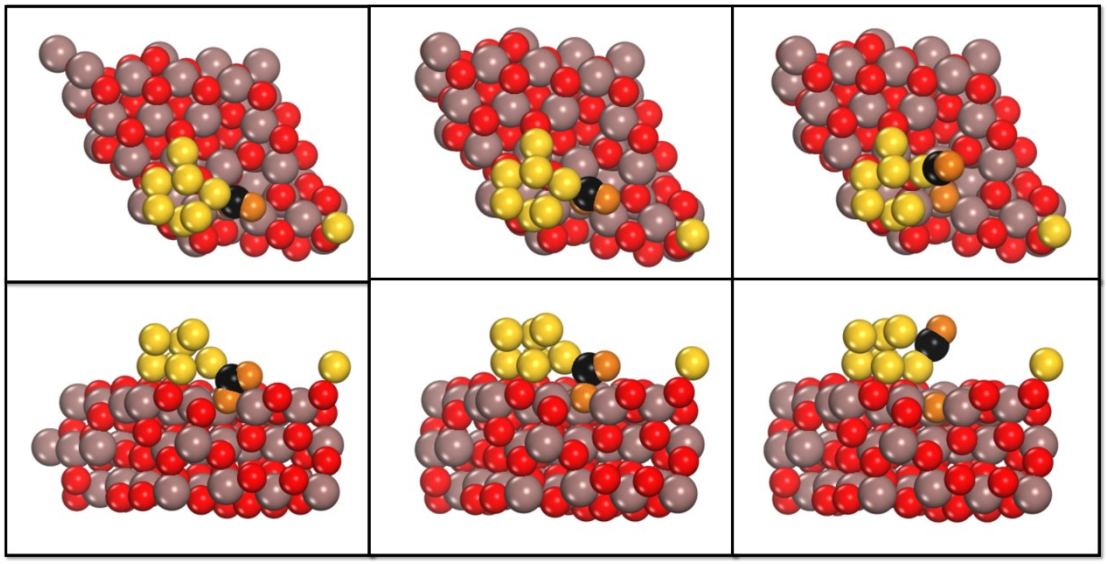

R10: CO*+O*+2H*→CO*+OH*+H*

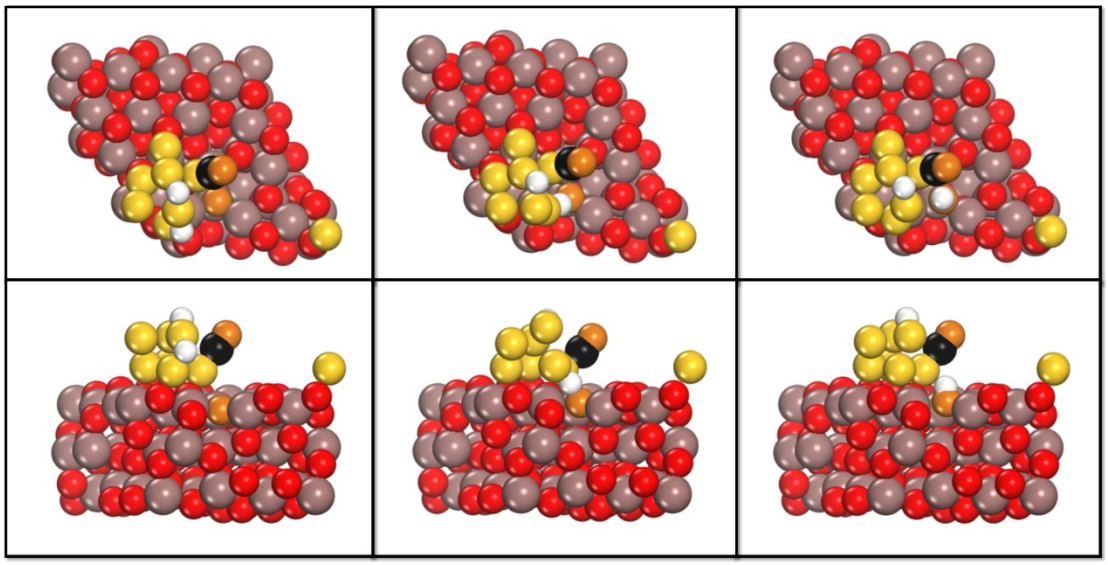

R11: CO*+OH*+H*→HCO*+OH*

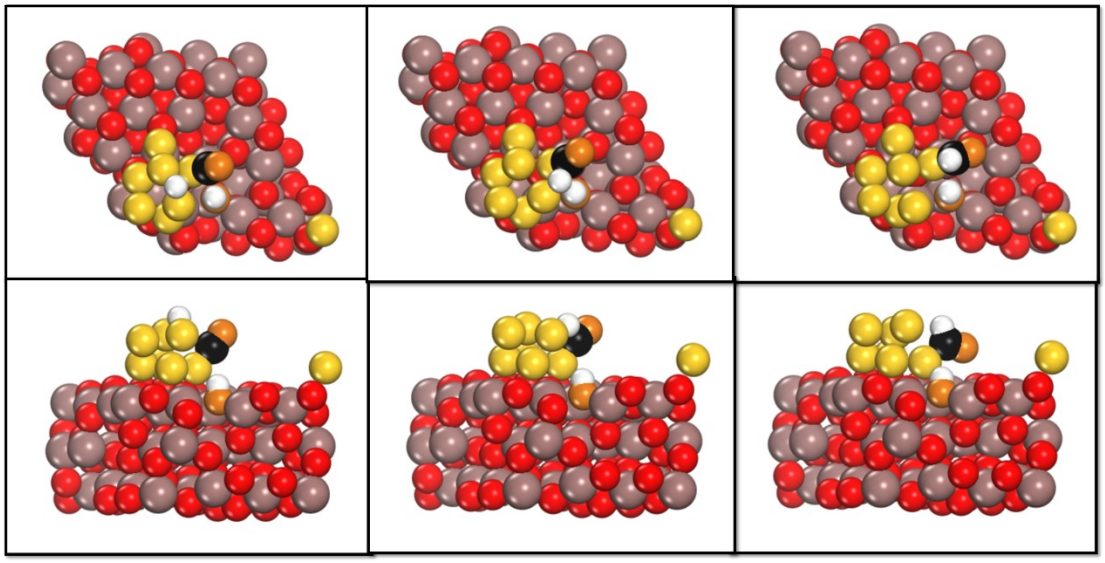

R12: $HCO^*+OH^*+2H^* \rightarrow HCO^*+H_2O^*+H^*$

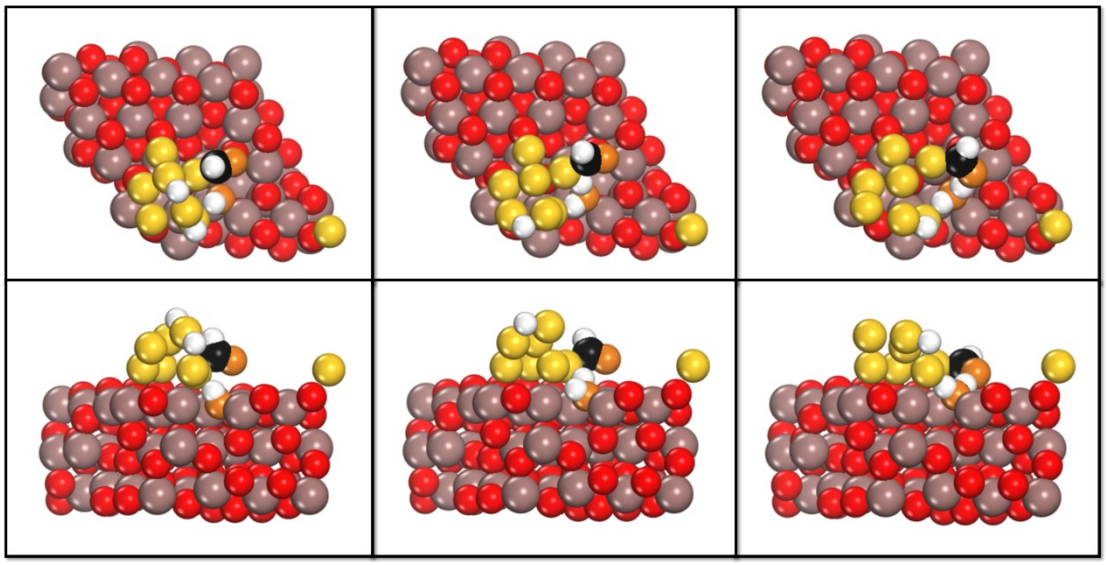

R13: $HCO^* +H^* \rightarrow H_2CO^*$

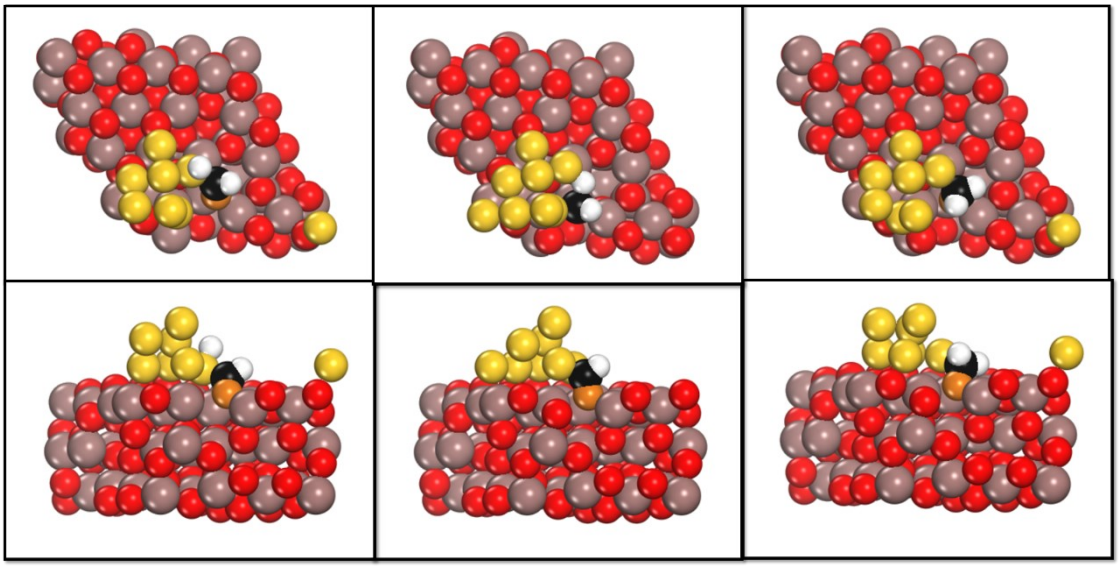

Fig. S11. Optimized configuration for each elementary step along the CO hydrogenation pathway over the Au_8/In_2O_3_d model.

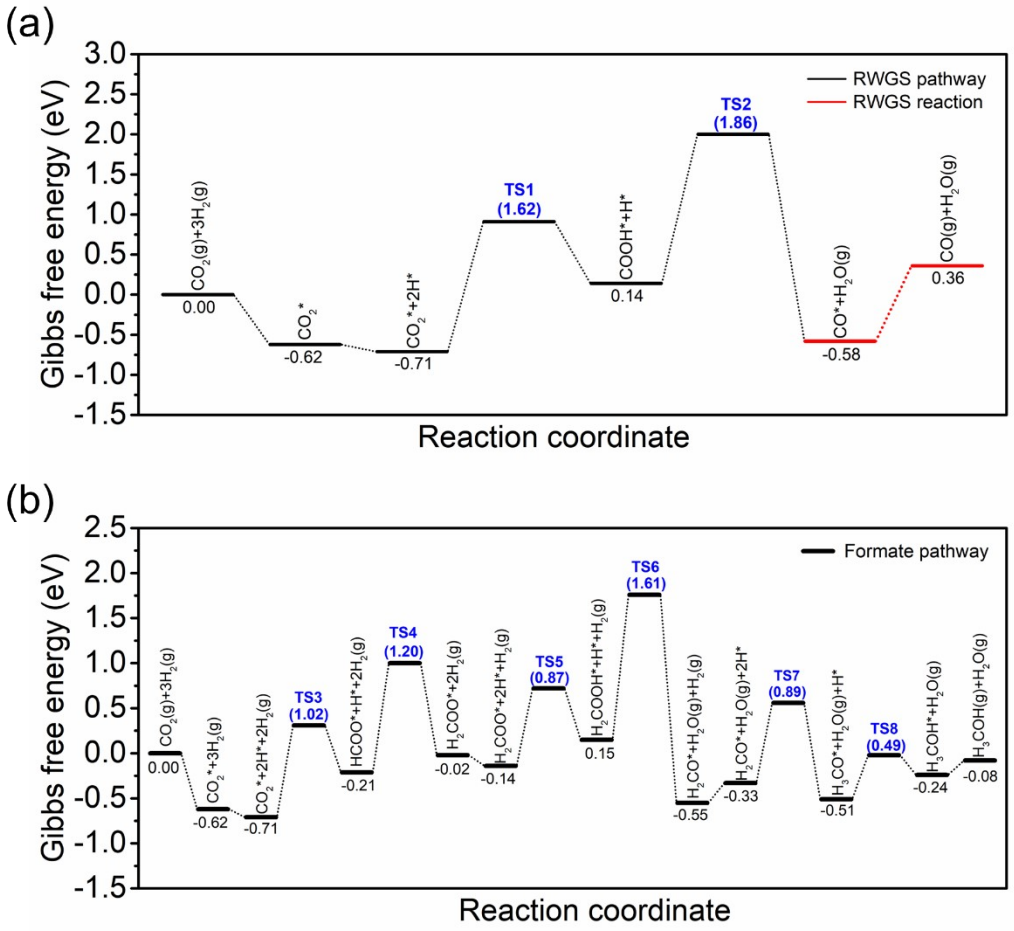

Fig. S12. Gibbs free energy profile for CO_2-to-methanol conversion on the Au_8/In_2O_3_d model via (a) the RWGS pathway and (b) the formate pathway at 300 °C and 5 MPa. "TS" corresponds to the transition state, and the value in parentheses represents the activation barrier.

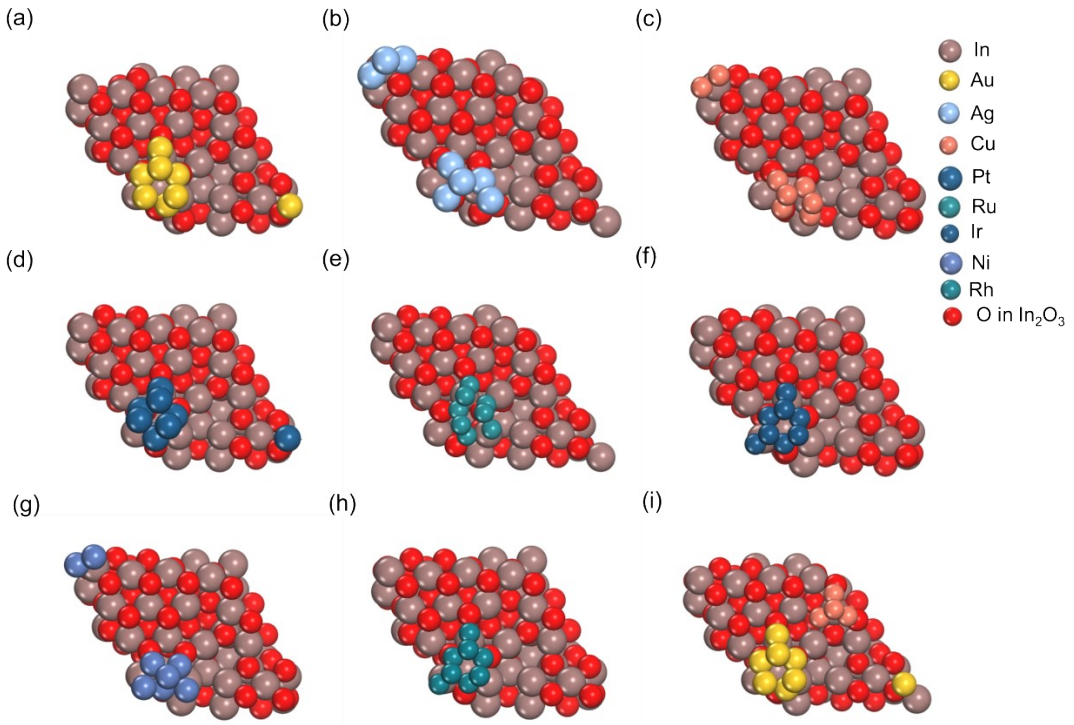

Fig. S13. Optimized configurations of the (a) Au_8/In_2O_3_d, (b) Ag_8/In_2O_3_d, (c) Cu_8/In_2O_3_d, (d) Pt_8/In_2O_3_d, (e) Ru_8/In_2O_3_d, (f) Ir_8/In_2O_3_d, (g) Ni_8/In_2O_3_d, (h) Rh_8/In_2O_3_d, (i) Au_8-Cu_4/In_2O_3_d.

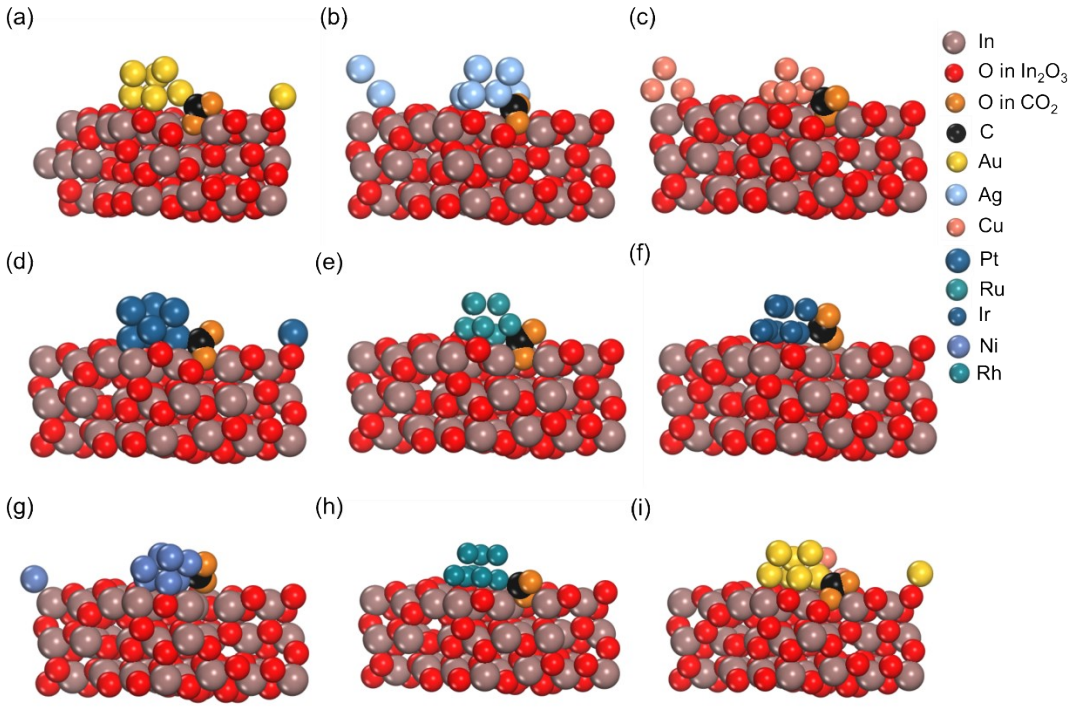

Fig. S14. Optimized configurations of the CO_2 adsorption on the interface of the (a) Au_8/In_2O_3_d, (b) Ag_8/In_2O_3_d, (c) Cu_8/In_2O_3_d, (d) Pt_8/In_2O_3_d, (e) Ru_8/In_2O_3_d, (f) Ir_8/In_2O_3_d, (g) Ni_8/In_2O_3_d, (h) Rh_8/In_2O_3_d, (i) Au_8-Cu_4/In_2O_3_d.

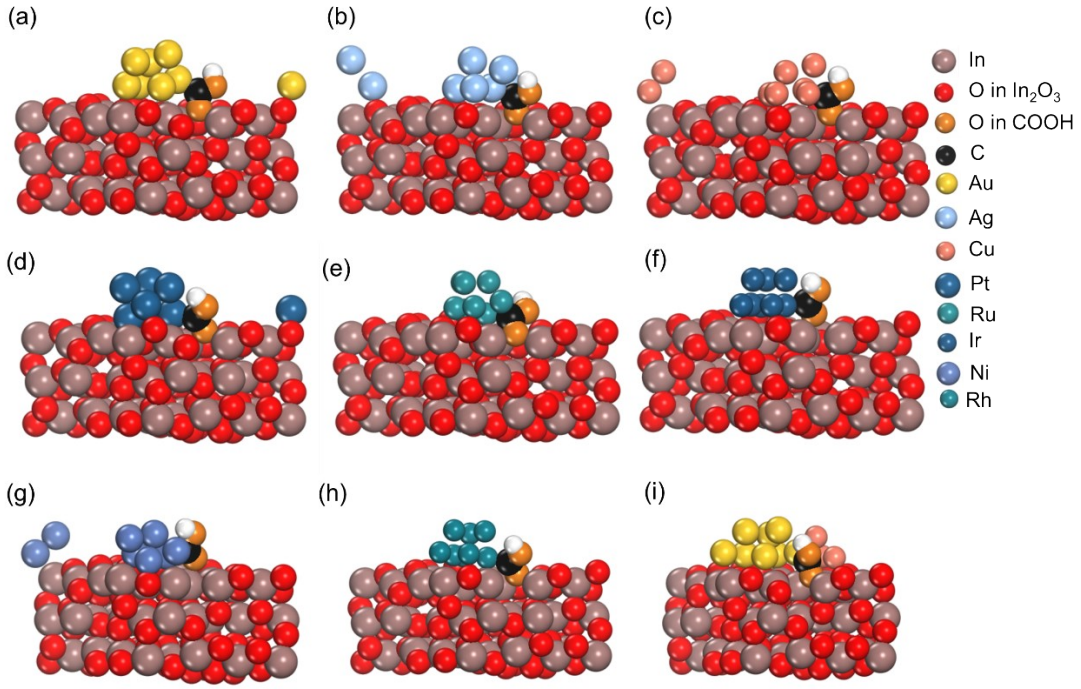

Fig. S15. Optimized configurations of the COOH adsorption on the interface of the (a) Au_8/In_2O_3_d, (b) Ag_8/In_2O_3_d, (c) Cu_8/In_2O_3_d, (d) Pt_8/In_2O_3_d, (e) Ru_8/In_2O_3_d, (f) Ir_8/In_2O_3_d, (g) Ni_8/In_2O_3_d, (h) Rh_8/In_2O_3_d, (i) Au_8-Cu_4/In_2O_3_d.

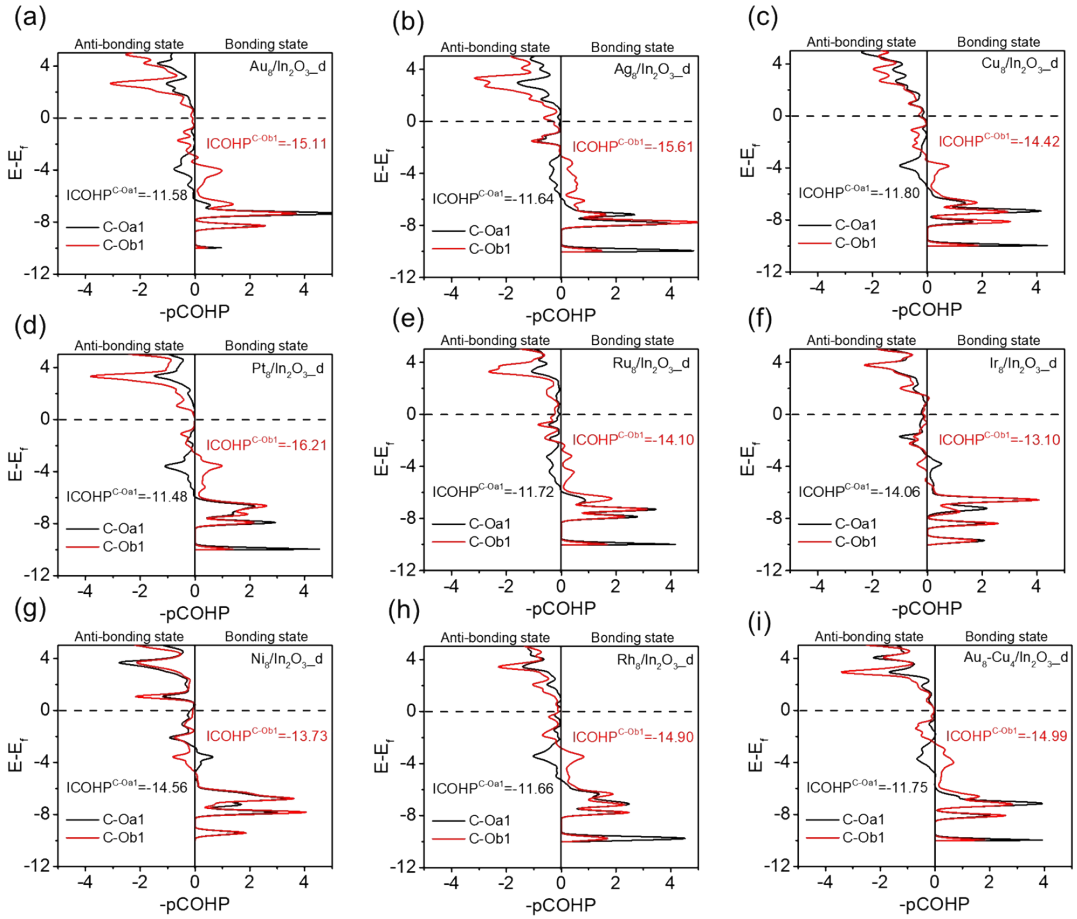

Fig. S16. Crystal orbital Hamilton populations (COHP) analysis for CO_2 adsorption on the interface of (a) Au_8/In_2O_3_d, (b) Ag_8/In_2O_3_d, (c) Cu_8/In_2O_3_d, (d) Pt_8/In_2O_3_d, (e) Ru_8/In_2O_3_d, (f) Ir_8/In_2O_3_d, (g) Ni_8/In_2O_3_d, (h) Rh_8/In_2O_3_d, (i) Au_8-Cu_4/In_2O_3_d.

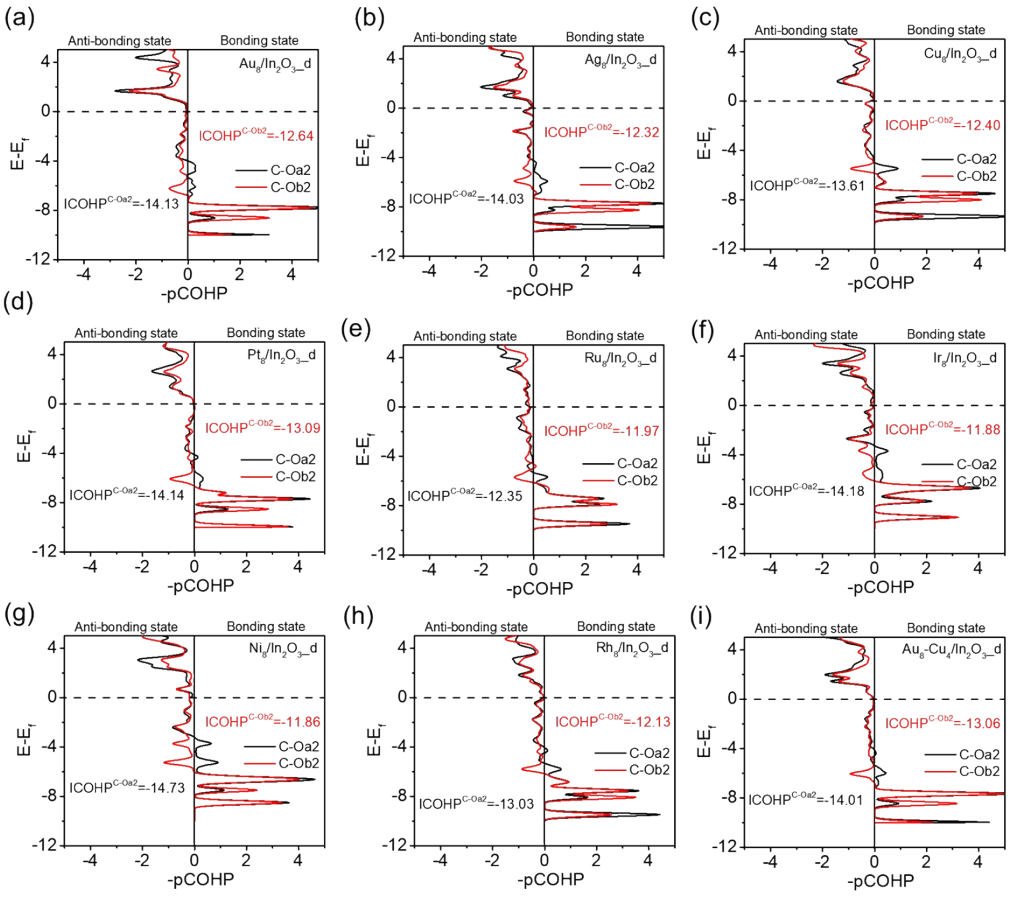

Fig. S17. Crystal orbital Hamilton populations (COHP) analysis for COOH adsorption on the interface of (a) Au_8/In_2O_3_d, (b) Ag_8/In_2O_3_d, (c) Cu_8/In_2O_3_d, (d) Pt_8/In_2O_3_d, (e) Ru_8/In_2O_3_d, (f) Ir_8/In_2O_3_d, (g) Ni_8/In_2O_3_d, (h) Rh_8/In_2O_3_d, (i) Au_8-Cu_4/In_2O_3_d.

CO-hydrogenation:

R14: CO_2*→CO*+O*

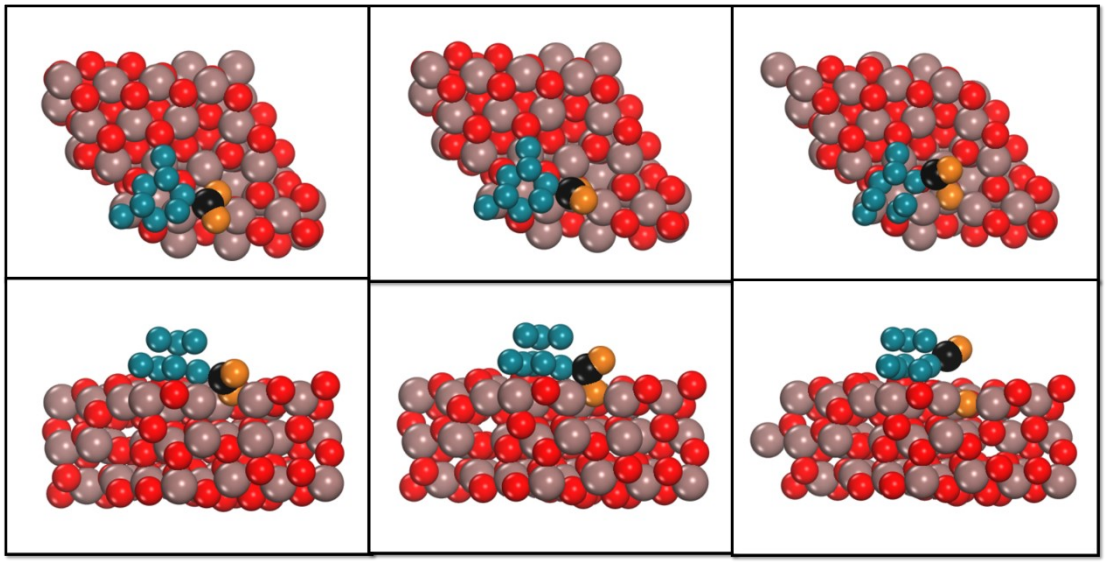

R15: CO*+O*+2H*→CO*+OH*+H*

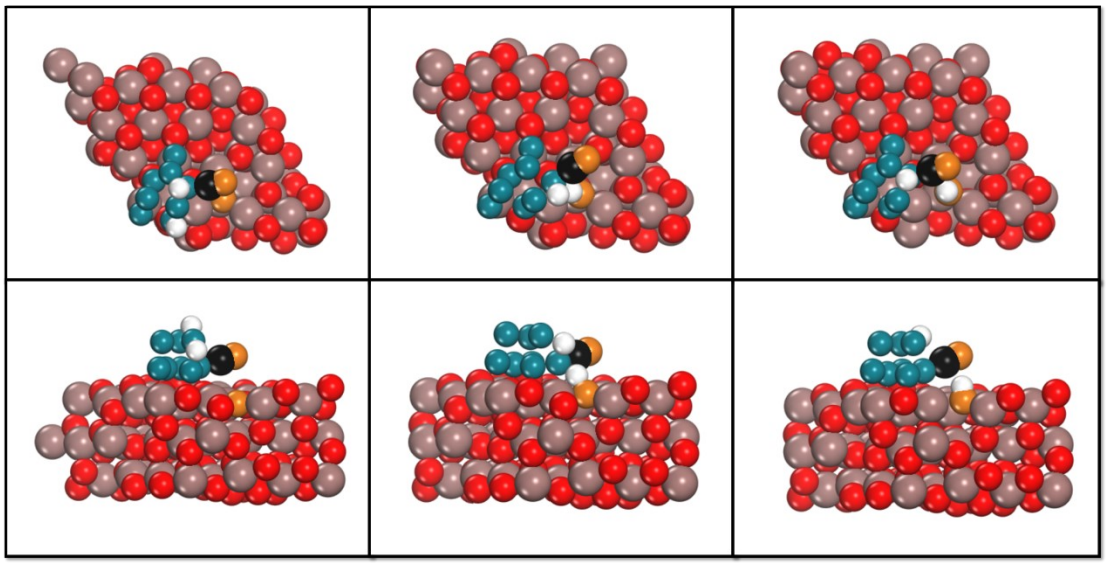

R16: CO*+OH*+H*→HCO*+OH*

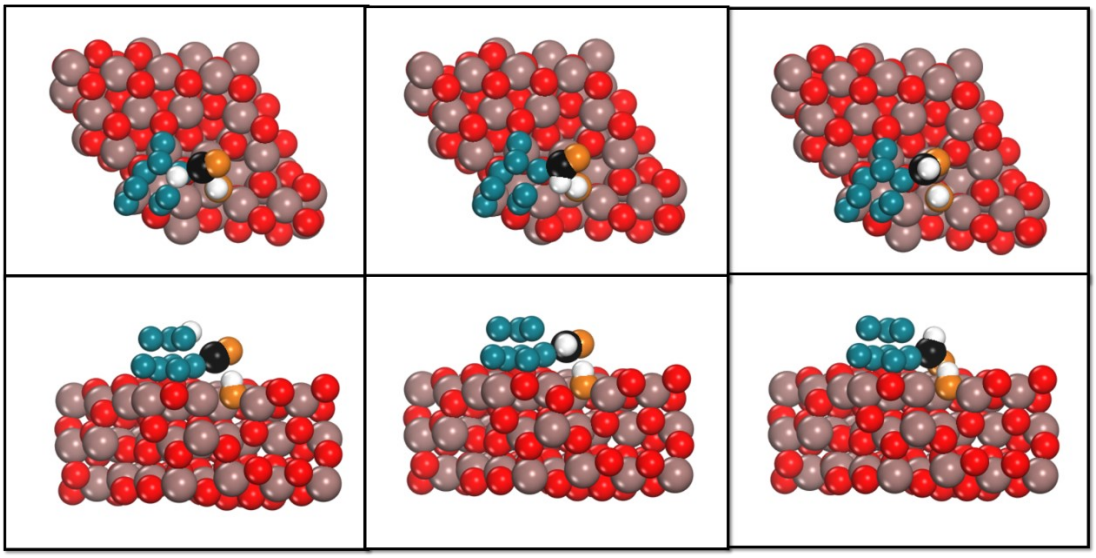

R17: $HCO^*+OH^*+2H^* \rightarrow HCO^*+H_2O^*+H^*$

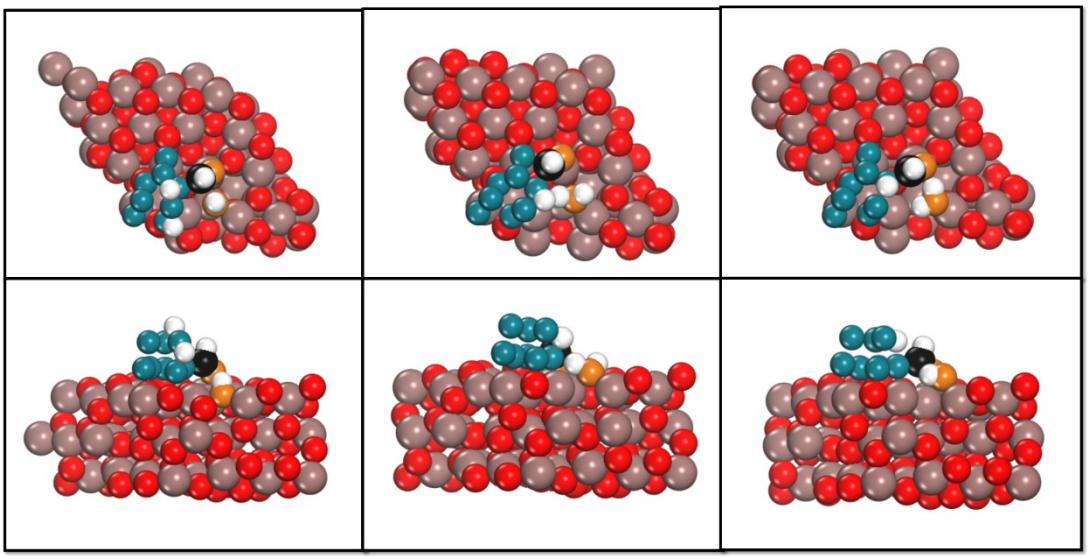

R18: $HCO^*+H^* \rightarrow H_2CO^*$

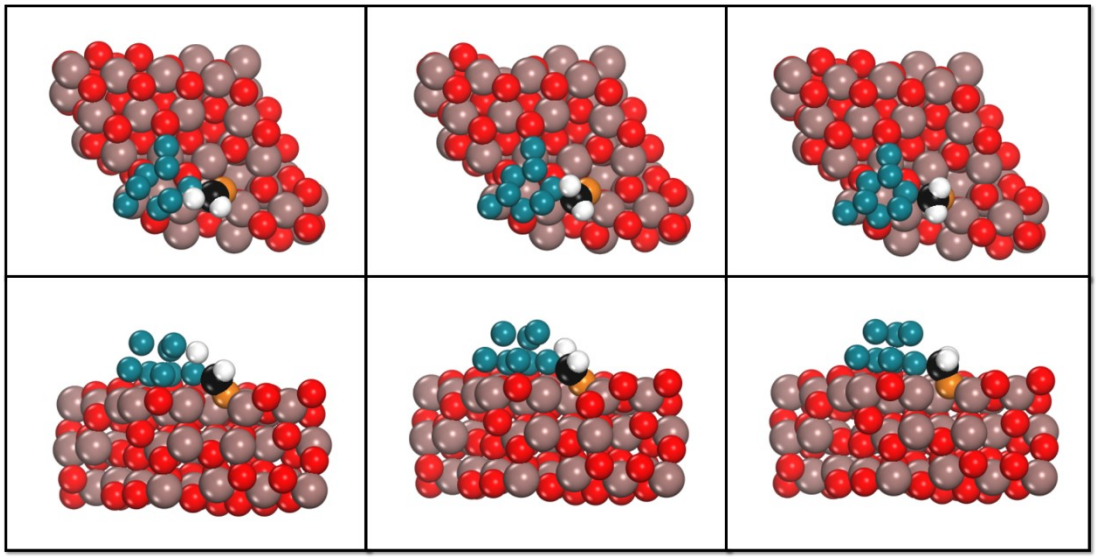

R19: $H_2CO^* + 2H^* \rightarrow H_3CO^*+H^*$

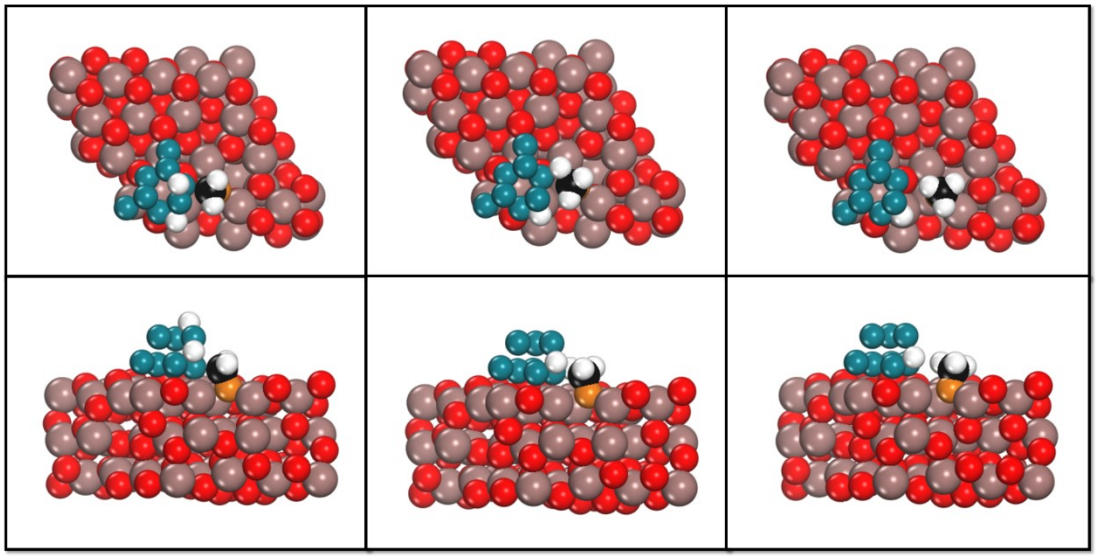

R20: $H_3CO^*+H^* \rightarrow H_3COH^*$

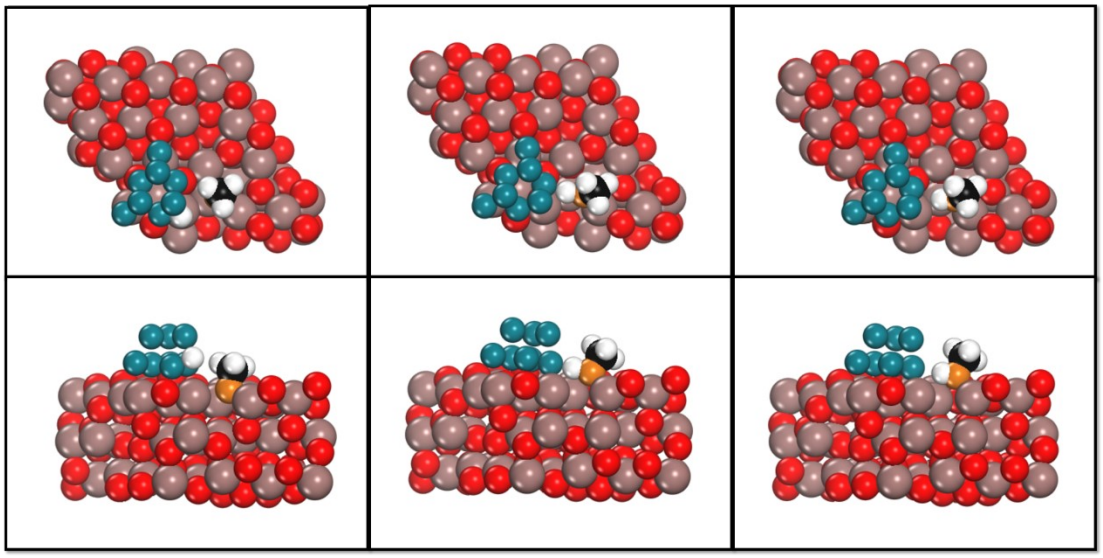

R21: CO_2*+2H*→HCOO*+H*

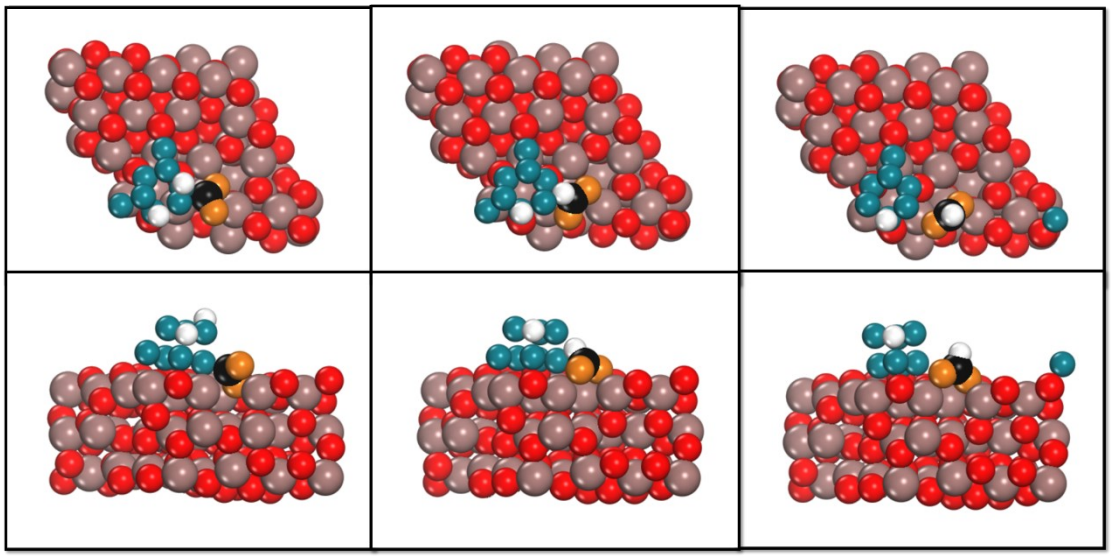

R21: CO_2*+2H*→COOH*+H*

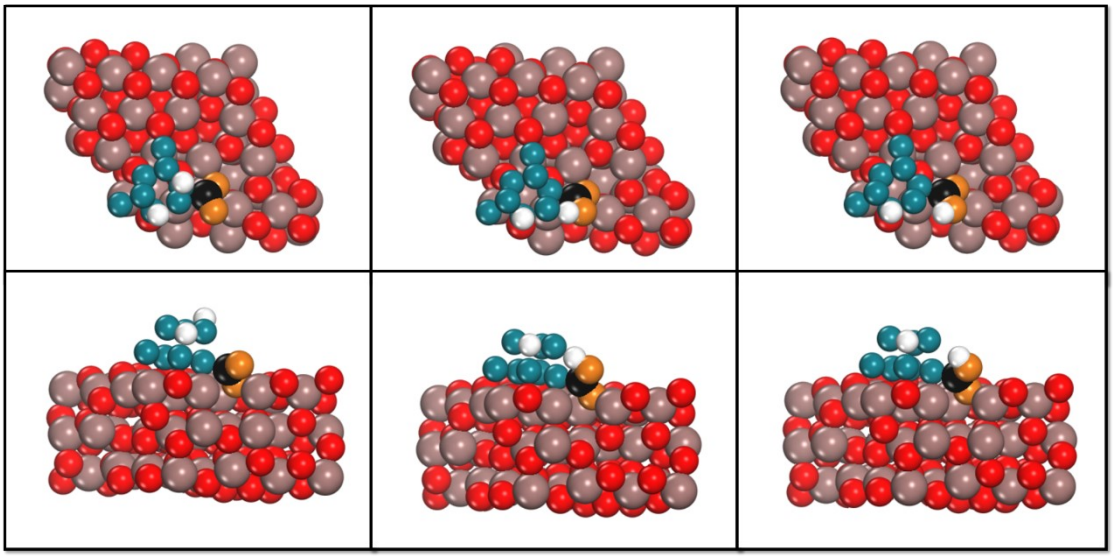

Fig. S18. Structures of all initial, transition, and final states for CO_2 hydrogenation to methanol on the Rh_8/In_2O_3_d model.

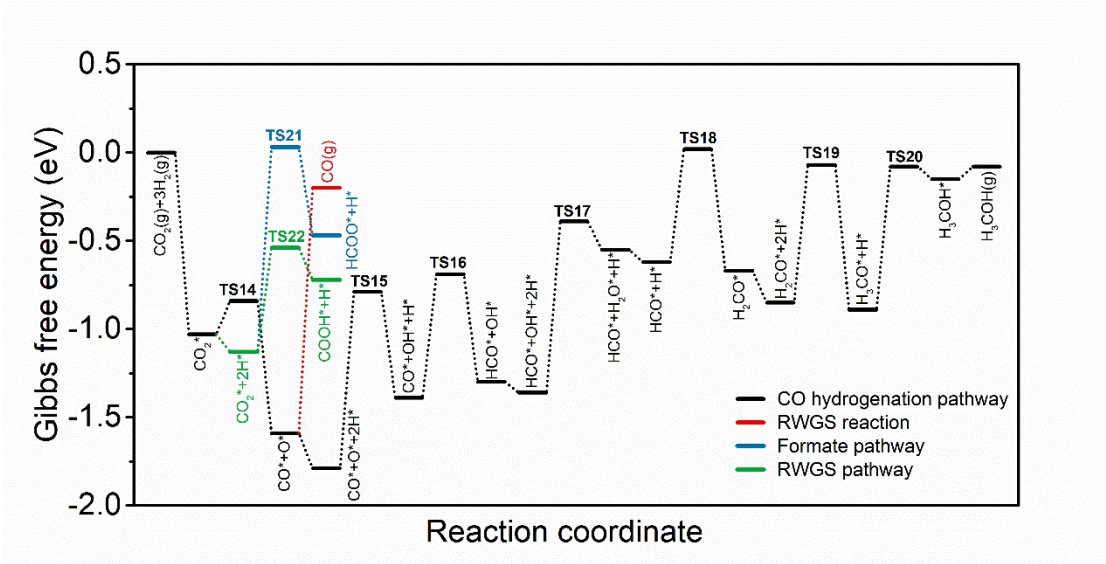

Fig. S19. Gibbs free energy profile for CO_2-to-methanol conversion on the Rh_8/In_2O_3_d model at 300 °C and 5 MPa.

Table S1. BET surface area and Au loading on Au(NC)/In_2O_3 and Au(NP)/In_2O_3.

	S_{BET} (m^2/g)	Au loading (wt%)
Au(NC)/In_2O_3	76	0.98
Au(NP)/In_2O_3	65	0.95

Table S2. EXAFS fitting parameters at the Au L_3-edge for Au(NC)/In_2O_3 (S_0^2=0.83 from Au-foil)

Catalyst	shell	CN [a]	*R* [b] (Å)	ΔE_0 [d] (eV)	*R* factor	σ^{2c} ($Å^2$)
Au(NC)/In_2O_3	Au−O	3.2±0.3	2.03±0.01	9.3±1.3	0.0120	0.0074
	Au−Au	4.4±0.4	2.82±0.01			0.0018
Au-foil	Au−Au	12	2.86±0.01	4.7±0.5	0.0040	0.0080

[a]*CN*: coordination numbers; [b]*R*: bond distance; [c]σ^2: Debye-Waller factors; [d] ΔE_0: the inner potential correction. R factor: goodness of fit. Error bounds that characterize the structural parameters obtained by EXAFS spectroscopy were estimated as CN±20%; R±1%; σ^2±20%.

Table S3. Energy of Au_8 isomers in the gas phase.

Configuration	Energy (eV)	Configuration	Energy (eV)
a	-17.61	g	-17.58
b	-17.59	h	-17.51
c	-17.37	i	-17.54
d	-17.32	j	-17.53
e	-17.49	k	-17.10
f	-17.43		

Table S4. ICOHP values of C-O bond for C-Oa1, C-Ob1 for adsorbed CO_2, and C-Oa2, C-Ob2 for adsorbed COOH.

	C-Oa1	C-Ob1	C-Oa2	C-Ob2
Au_8/In_2O_3_d	-11.58	-15.11	-14.13	-12.64
Ag_8/In_2O_3_d	-11.64	-15.61	-14.03	-12.32
Cu_8/In_2O_3_d	-11.80	-14.42	-13.61	-12.40
Pt_8/In_2O_3_d	-11.48	-16.21	-14.14	-13.09
Ru_8/In_2O_3_d	-11.72	-14.10	-12.35	-11.97
Ir_8/In_2O_3_d	-14.06	-13.10	-14.18	-11.88
Ni_8/In_2O_3_d	-14.56	-13.73	-14.73	-11.86
Rh_8/In_2O_3_d	-11.66	-14.90	-13.03	-12.13
Au_8-Cu_4/In_2O_3_d	-11.75	-14.99	-14.01	-13.06

Table S5. Experimental turnover frequencies (TOFs) of methanol at 250 °C and GHSV = 21,000 $cm^3\ h^{-1}\ g_{cat}^{-1}$ and relevant information for the seven reported metal-promoted In_2O_3 catalysts for CO_2 hydrogenation to methanol

	Metal loading (wt%)	STY of methanol ($g_{MeOH}\ g_{cat}^{-1}\ h^{-1}$)	TOF (s^{-1})	Ref.
Au/In_2O_3	0.98	0.182	0.031	S14
Ag/In_2O_3	0.33	0.104	0.030	S16
Cu/In_2O_3	1.00	0.150	0.010	S15
Pt/In_2O_3	1.07	0.316	0.050	S11(a)
Ru/In_2O_3	1.10	0.167	0.013	S17
Ir/In_2O_3	10.00	0.309	0.005	S18
Ni/In_2O_3	10.00	0.213	0.001	S19
Rh/In_2O_3	1.07	0.188	0.016	S20
$Au\text{-}Cu/In_2O_3$	1.93	0.260	0.011	S15

REFERENCE

S1. J. P. Perdew, K. Burke and M. Ernzerhof, *Phys. Rev. Lett.*, 1996, **77**, 3865-3868.

S2. G. Kresse and D. Joubert, *Phys. Rev. B*, 1998, **59**, 1758-1775.

S3. S. Grimme, J. Antony, S. Ehrlich and H. Krieg, *J. Chem. Phys.*, 2010, **132**, 154104.

S4. G. Henkelman, B. P. Uberuaga and H. Jónsson, *J. Chem. Phys.*, 2000, **113**, 9901-9904.

S5. G. Henkelman and H. Jónsson, *J. Phys. Chem. C*, 1999, **111**, 7010-7022.

S6. A. Cao, Z. Wang, H. Li and J. K. Nørskov, *ACS Catal.*, 2021, **11**, 1780-1786.

S7. (a) J. Ye, C. Liu, D. Mei and Q. Ge, *ACS Catal.*, 2013, **3**, 1296-1306; (b) R. Zou, C. Shen, K. Sun, X. Ma, Z. Li, M. Li and C.-J. Liu, *J. Energy Chem.*, 2024, **93**, 135-145; (c) W. Wang, Y. Chen and M. Zhang, *Surf. Interfaces*, 2021, **25**, 101244.

S8. K. Sun, M. Kohyama, S. Tanaka and S. Takeda, *J. Phys. Chem. C*, 2014, **118**, 1611-1617.

S9. (a) V. Wang, N. Xu, J.-C. Liu, G. Tang and W.-T. Geng, *Comput. Phys. Commun.*, 2021, **267**, 108033; (b) R. Zou, K. Sun, C. Shen and C.-J. Liu, *Phys. Chem. Chem. Phys.*, 2022, **24**, 25522-25529.

S10. S. Maintz, V. L. Deringer, A. L. Tchougréeff and R. Dronskowski, *J. Comput. Chem.*, 2016, **37**, 1030-1035.

S11. (a) K. Sun, N. Rui, Z. Zhang, Z. Sun, Q. Ge and C.-J. Liu, *Green Chem.*, 2020, **22**, 5059-5066; (b) L. Wu, R. Zou, C. Shen and C.-j. Liu, *Energy Fuels*, 2023, **37**, 18120-18127.

S12. F. Cárdenas-Lizana and M. A. Keane, *J. Mater. Sci.*, 2012, **48**, 543-564.

S13. B. Ravel; M. Newville, *J. Synchrotron Radiat.*, 2005, **12,** 537-541.

S14. N. Rui, F. Zhang, K. Sun, Z. Liu, W. Xu, E. Stavitski, S. D. Senanayake, J. A. Rodriguez and C.-J. Liu, *ACS Catal.*, 2020, **10**, 11307-11317.

S15. R. Zou, M. Liu, L. Wu, C. Shen, Z. Li, X. Ma, M. Li and C.-j. Liu, *J. Energy Chem.*, 2026, **113**, 852-863.

S16. K. Sun, Z. Zhang, C. Shen, N. Rui and C.-j. Liu, *Green Energy Environ.*, 2022, **7**, 807-817.

S17. Q. Wu, C. Shen, N. Rui, K. Sun and C.-j. Liu, *J. CO2 Util.*, 2021, **53**, 101720.

S18. C. Shen, K. Sun, Z. Zhang, N. Rui, X. Jia, D. Mei and C.-j. Liu, *ACS Catal.*, 2021, **11**, 4036-4046

S19. X. Jia, K. Sun, J. Wang, C. Shen and C.-j. Liu, *J. Energy Chem.*, 2020, **50**, 409-415

S20. J. Wang, K. Sun, X. Jia and C.-j. Liu, Catal. Today, 2021, 365, 341-347